

## EXTREME ULTRAVIOLET EXPLORER SPECTRA OF THE 1993 MARCH FLARES ON AD LEONIS: THE DIFFERENTIAL EMISSION MEASURE AND IMPLICATIONS FOR CORONAL STRUCTURE

SCOTT L. CULLY

Experimental Astrophysics Group, Space Sciences Laboratory, University of California, Berkeley, Berkeley, CA 94720-7450

GEORGE H. FISHER

Space Sciences Laboratory, University of California, Berkeley, Berkeley, CA 94720-7450

SUZANNE L. HAWLEY<sup>1</sup>

Department of Physics and Astronomy, Michigan State University, East Lansing, MI 48824

AND

THEODORE SIMON

Institute for Astronomy, University of Hawaii, 2680 Woodlawn Drive, Honolulu, HI 96822

Received 1997 April 2; accepted 1997 August 4

### ABSTRACT

The flare star AD Leonis was observed by the *Extreme Ultraviolet Explorer* (*EUVE*) from 1993 March 1 to 3 UT. Two flares were detected by the *EUVE* Deep Survey detector and spectrometer and also seen in optical photometry on 1993 March 2 UT. The DS Lexan/boron-band and optical results have been discussed in the previous paper by Hawley et al. In this paper, we describe the spectra observed by *EUVE* during quiescence, the peaks of the flares, and the decay phase following the first flare and analyze the spectra to investigate the stellar atmospheric structure during these time periods.

The spectra show that the observed EUV emission from AD Leo is dominated by iron lines from a hot coronal plasma. Two methods were used to estimate the differential emission measure distribution (DEM) of the stellar corona. In the “Pottasch” method, we fitted Gaussian line profiles to the strongest lines in the spectra and estimated the DEM at the formation temperature of those lines. Upper limits to the DEM were obtained in the case of no detection. We also used a regularized inversion technique, together with a weighting scheme based on information contained in the plasma-emission model and on the signal-to-noise ratio of the data, to find the DEM. The weighting was designed to prevent the noisy pixels in our low-signal-to-noise ratio data from dominating the solution. The results produced by the two methods are consistent in the temperature regimes where strong lines are present. The inversion method provides additional information where no strong single lines dominate the spectra. The ability to use lines from the entire wavelength region covered by the spectra allowed us to investigate the hydrogen column  $N_{\text{H}}$  and iron abundance  $[\text{Fe}/\text{H}]$ .

We found that  $[\text{Fe}/\text{H}]$  in the corona of AD Leo was essentially unconstrained by our data, but  $N_{\text{H}}$  was well determined, yielding  $N_{\text{H}} \sim (3 \pm 1) \times 10^{18} \text{ cm}^{-2}$ . We assumed both a solar-coronal value of  $[\text{Fe}/\text{H}]$  and a value one tenth of this and computed the DEM distribution of the stellar corona for both cases.

The DEM of the quiescent corona is dominated by a broad plateau of emission ranging from  $10^{6.8}$  to  $10^{7.2}$  K, with the DEM of plasma near  $10^{6.2}$  K about an order of magnitude less. We interpret the plateau of the DEM in terms of a broad distribution of loops with differing peak temperatures. We discuss and compare these results with those of Giampapa et al., who analyzed *ROSAT* soft X-ray data from AD Leo taken during a different time period.

The DEM of the flare plasma is strongly peaked at temperatures greater than  $10^7$  K, indicative of hot flare loops, while that of the decay phase consists of a smaller peak at temperatures less than  $10^7$  K, as might be expected from the cooling and condensation of previously heated flare loops. These results are consistent with a flare model that includes strong evaporation and condensation as in our previous paper. The *EUVE* spectral analysis leads to lower peak flare temperatures than those used in our previous paper, but the basic conclusion reached—that the dominant flaring emission originates from long loops with  $L \sim R_*$  and with peak flare densities ranging from  $10^9$  to  $10^{11} \text{ cm}^{-3}$ —remains unchanged. This conclusion is not qualitatively affected by the value of  $[\text{Fe}/\text{H}]$  used in our DEM analysis.

*Subject headings:* stars: coronae — stars: flare — stars: individual (AD Leo) — ultraviolet: stars

### 1. INTRODUCTION

The flare star AD Leonis (dM3e,  $d = 4.9$  pc; Reid, Hawley, & Gizis 1995) was observed by the NASA *Extreme Ultraviolet Explorer* (*EUVE*) satellite using the Deep

Survey (DS) instrument and spectrometers (Malina & Bowyer 1991) from 06:00 UT 1993 March 1 to 23:21 UT 1993 March 3 as part of a coordinated campaign involving *EUVE* and 6 optical telescopes. Two flares were plainly visible in the light curve of the Lexan/boron (40–190 Å) band of the Deep Survey instrument, the first beginning at 08:24 UT March 2 and the second at 08:38 UT March 3

<sup>1</sup> NSF Young Investigator.

(Fig. 1). Flare 1 consisted of two separate events that formed a plateau of elevated count rate with a duration of roughly 7 hr. This peak was followed by an exponentially decaying tail of enhanced count rate that lasted approximately 15 hr. The second, smaller flare (flare 2) was observed for 2 hr, apparently superposed on the decay tail of flare 1. The light curve then returned to a quiescent state, interrupted by several much smaller flares.

In Hawley et al. (1995; hereafter Paper I), we analyzed the DS light curve together with the optical data and found evidence for a stellar Neupert effect (Dennis & Zarro 1993; Neupert 1968). We also applied the coronal loop models that we developed in Fisher & Hawley (1990) to enable us to derive coronal loop parameters (such as loop length and pressure) for these AD Leo flares. However, we had only a rough estimate of the coronal temperature, based on a quick inspection of the *EUVE* spectra, during the flares. The derived values of the loop length, pressure, and column depth depend on the peak temperature of the loop; it is therefore important to see whether the conclusions we reached in Paper I are changed as a result of the coronal temperatures we find here.

In this paper, we continue our analysis and interpretation of the AD Leo flares by examining in detail the *EUVE* SW (60–190 Å), MW (160–320 Å), and LW (300–760 Å) spectra taken during the peaks of the flares, the decay phase of flare 1, and the quiescent period before the beginning of flare 1 and after flare 2. In § 2 we describe the data reduction, including the optimal spectral extraction method, and present line identifications where possible. In § 3 we discuss the Pottasch method for estimating the differential emission measure (DEM). In § 4 we present the inversion technique that we used to produce continuous DEM distributions from the observed spectra and discuss the effects of an additional weighting function we introduced to accommodate the low signal-to-noise ratio (S/N) of the data. In § 5 we test the robustness of the inversion method using Monte Carlo simulations with a test DEM. In § 6, we give the results of the DEM analysis from both the Pottasch and inversion methods and comment on our attempts to find the hydrogen column density and the metal abundance simultaneously with the DEM. In § 7 we discuss the implications of our results for the coronal structure of AD Leo in quiescence

and during flares. We also compare our results with a recent study by Giampapa et al. (1996; hereafter G96). Finally, in § 8, we present our conclusions.

## 2. SPECTRAL EXTRACTION AND LINE IDENTIFICATION

We first divide our *EUVE* observation into the four temporal regions of interest using the *EUVE* IRAF-based software (EGODATA 1.8.1). The quiescent spectrum is defined as the measurements taken before the first flare and after the second flare, giving a total exposure time of approximately 70 ks. The sharp peaks of flare 1 and flare 2 define two more temporal cuts with exposure times of 13.2 and 3.4 ks respectively. The decay spectrum includes the period between the two flare peaks, when the emission is still enhanced from flare 1 and has a roughly 16 ks exposure time.

For each of the time periods, we obtain SW, MW, and LW spectra imaged onto the three separate microchannel plate (MCP) detectors. Along with the spectrum, each detector image included background noise from cosmic rays, the beta decay of  $K^{40}$  in the MCP glass (Siegmund, Vallerga, & Wargelin 1987), and geocoronal 304 and 584 Å emission. The geocoronal emission appeared as  $\sim 30$  Å wide strips running perpendicular to the dispersion direction in the MW and LW detector images (see Malina & Bowyer 1991 for discussion).

The standard procedure employed to correct for the background noise is to define a narrow rectangular region with area  $A_{\text{spec}}$  containing the spectrum plus background image,  $S$ , and two much larger regions equidistant above and below the spectrum with total area  $A_{\text{back}}$ , containing the background image  $B$ . The spectrum is found by simple background subtraction,

$$f_i = S_i - \frac{A_{\text{spec}}}{A_{\text{back}}} B_i \quad (1)$$

for each wavelength pixel  $i$ . The errors in each wavelength pixel are given by Poisson statistics,

$$\delta f_i = \sqrt{S_i + \left(\frac{A_{\text{spec}}}{A_{\text{back}}}\right)^2 B_i}. \quad (2)$$

Although this method works well for strong, source-dominated spectra, we found that our background-dominated spectra were so faint compared with the noise that only a few lines were visible. To improve the quality of the extracted data, we used an Interactive Data Language (IDL) optimal extraction routine based on the work of Horne (1986). We first binned the detector image by a factor of 4 in both the dispersion and cross-dispersion directions. (Four of the original detector pixels correspond to approximately one-half of a resolution element in wavelength; hereafter we refer to the  $4 \times 4$  bin of the original detector pixels as a “binned pixel.”) We then estimated the detector background counts by masking out the rows of binned pixels containing the spectrum, using a median filter to eliminate excessively high and low binned pixels in the background image, and then twice applying a  $7 \times 7$  binned-pixel boxcar-smoothing filter to the image. The smoothed background was subtracted from the spectral region to produce an estimate of the source spectrum (which is still two-dimensional at this point).

We then computed the normalized cross-dispersion profile,  $P_{\lambda,y}$ , of the spectra as a function of the cross-dispersion binned-pixel number  $y$  and rebinned the result

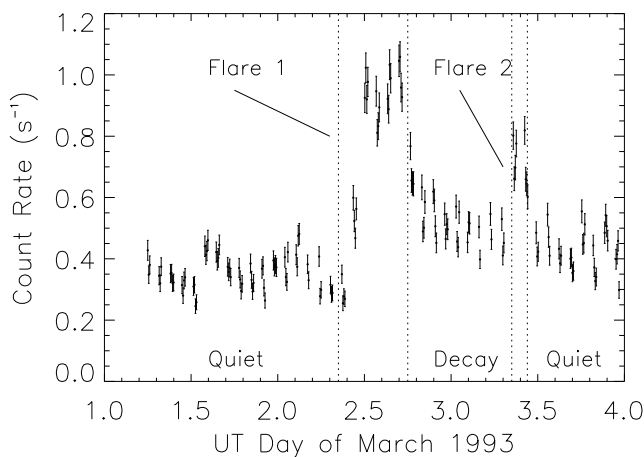


FIG. 1.—*EUVE* DS (Deep Survey Lexan/Boron 40–190 Å) light curve showing the four time periods of our observation. The spectra discussed in the paper are analyzed for each of these time periods.

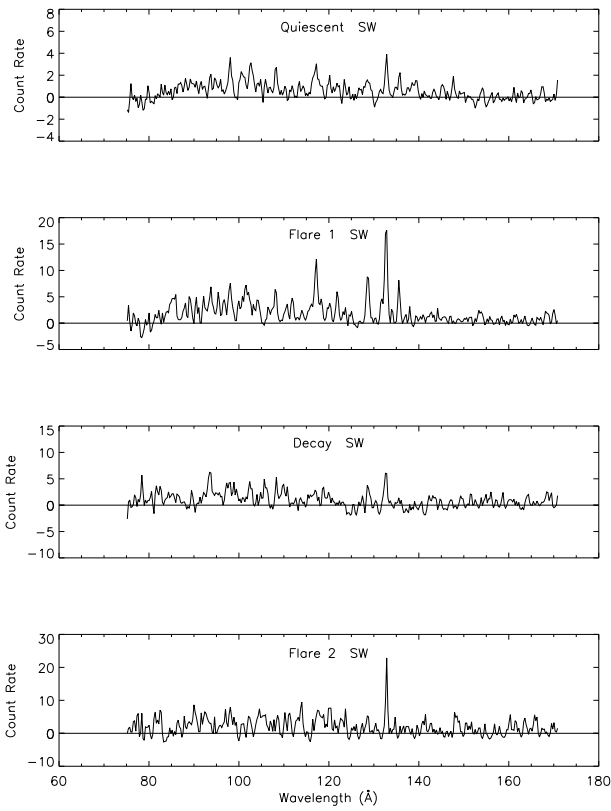


FIG. 2a

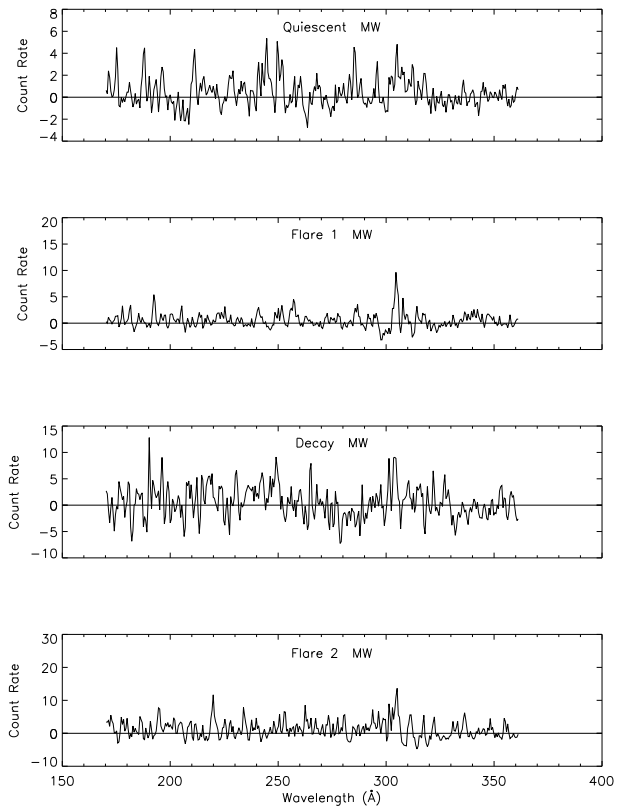


FIG. 2b

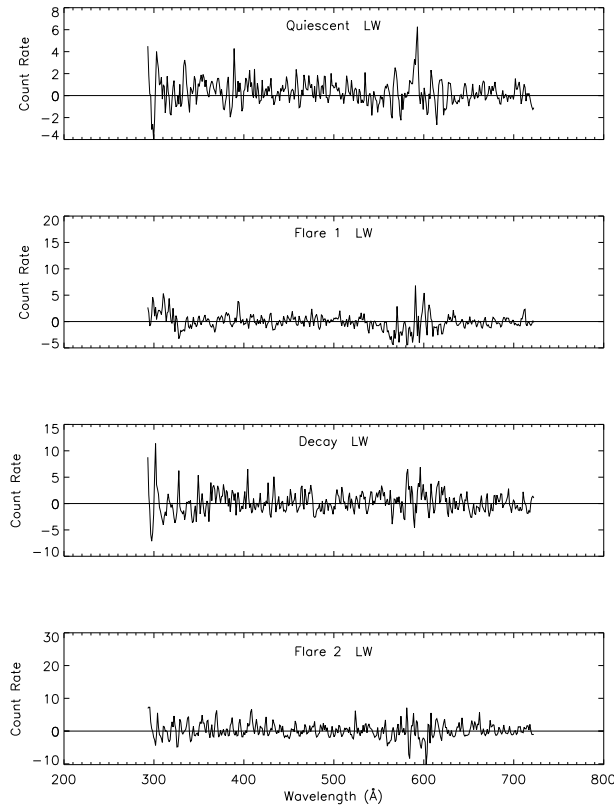


FIG. 2c

FIG. 2.— Count-rate spectra for the four time periods shown in Fig. 1. Values in each figure must be multiplied by  $10^{-4}$  to convert to counts  $s^{-1}$ . For each detector, the variation of S/N with wavelength is similar to that of the count rate itself, with peak S/N values for the quiescent, flare 1, decay, and flare 2 periods, respectively, of (a) 3, 4, 2.5, and 2.5 for the SW detector; (b) 3, 2.5, 3, and 2 for the MW detector; and (c) 3, 2, 2.5, and 2 for the LW detector.

TABLE 1  
OBSERVED DATA FOR UNAMBIGUOUS SPECTRAL LINES

WAVELENGTH (Å)	DETECTOR	ION	$\log_{10} T$	QUIET			FLARE 1			DECAY			FLARE 2		
				Count Flux <sup>a</sup> ( $10^{-4}$ counts $s^{-1} \text{ cm}^{-2}$ )	S/N	FWHM (Å)	Count Flux <sup>a</sup> ( $10^{-4}$ counts $s^{-1} \text{ cm}^{-2}$ )	S/N	FWHM (Å)	Count Flux <sup>a</sup> ( $10^{-4}$ counts $s^{-1} \text{ cm}^{-2}$ )	S/N	FWHM (Å)	Count Flux <sup>a</sup> ( $10^{-4}$ counts $s^{-1} \text{ cm}^{-2}$ )	S/N	FWHM (Å)
93.3	SW	Fe XVIII	6.8	3.2	2.20	0.65	10.5	2.80	0.65	10.3	3.00	0.65	<22.4	...	...
108.4	SW	Fe XIX	6.9	5.0	3.10	0.74	11.2	3.30	0.70	6.6	2.20	0.54	<23.4	...	...
116.3	SW	Fe XXII	7.1	<4.5	...	...	<10.2	...	...	<8.9	...	...	<27.4	...	...
117.2	SW	Fe XXII	7.1	5.9	3.10	0.75	25.5	5.20	0.75	<8.9	...	...	<28.2	...	...
118.7	SW	Fe XX	6.9	<4.3	...	...	10.1	2.40	0.75	<9.1	...	...	<28.3	...	...
121.6	SW	Fe XX	6.9	<4.4	...	...	13.8	3.00	0.74	<9.3	...	...	<30.7	...	...
128.7	SW	Fe XXI	7.0	4.9	2.10	0.74	27.9	4.20	0.74	8.9	2.00	0.56	<38.2	...	...
132.8	SW	Fe XXIII/XX	7.2	10.4	3.80	0.62	59.5	6.70	0.69	15.4	2.70	0.50	<35.5 <sup>b</sup>	...	0.26
135.8	SW	Fe XXII	7.1	7.5	2.60	0.64	23.1	3.50	0.58	<13.5	...	...	<49.2	...	...
171.1	MW	Fe IX/O V	5.8	<11.3	...	...	<13.8	...	...	<29.2	...	...	<47.7	...	...
174.5	SW	Fe X	6.0	<23.9	...	...	<15.1	...	...	<27.1	...	...	<47.7	...	...
177.2	MW	Fe X	6.0	<10.4	...	...	<15.5	...	...	<30.3	...	...	<48.3	...	...
180.6	MW	Fe XI	6.1	<10.8	...	...	<70.5	...	...	<66.9	...	...	<265.0	...	...
192.0	MW	Fe XXIV/O V	7.2	<11.4	...	...	<19.1	...	...	<31.8	...	...	<49.3	...	...
202.1	MW	Fe XIII	6.2	<11.1	...	...	<15.3	...	...	<33.1	...	...	<52.0	...	...
238.5	MW	O IV	5.3	<13.5	...	...	<17.4	...	...	<41.7	...	...	<62.5	...	...
255.1	MW	Fe XXIV	7.2	<13.5	...	...	<23.7	...	...	<40.9	...	...	<67.2	...	...
284.2	MW	Fe XV	6.3	18.5	3.00	1.48	<18.8	...	...	<35.3	...	...	<69.1	...	...
303.9	MW	He II	4.9	24.2	2.70	1.48	57.5	3.40	1.83	59.5	2.70	1.48	120.0	2.50	3.31
335.4	LW	Fe XVI	6.4	16.0	2.90	3.49	<19.3	...	...	<22.3	...	...	<51.4	...	...
358.9	LW	Ne V	5.5	<8.7	...	...	<14.7	...	...	<17.6	...	...	<47.8	...	...
401.7	LW	Ne VI	5.7	<12.1	...	...	<18.5	...	...	<26.9	...	...	<66.3	...	...
554.4	LW	O IV	5.3	<20.9	...	...	<35.2	...	...	<47.9	...	...	<117.0	...	...
584.4	LW	He I	4.5	<78.3	...	...	<147.0	...	...	<144.0	...	...	<275.0	...	...

<sup>a</sup> Observed photon count rate corrected for instrumental response.

<sup>b</sup> Small width may indicate spurious detection. See text.

into four equal wavelength bins spanning the wavelength range of each of the three spectral images. If the S/N in any cross-dispersion profile was inadequate ( $< 2\sigma$ ), we substituted a composite profile computed from the continuum spectra of several white dwarfs. The cross-dispersion profiles were used to compute the optimally extracted, one-dimensional spectra:

$$f_{\lambda}^{\text{opt}} = \frac{\sum_y P_{\lambda,y}(S_{\lambda,y} - B_{\lambda,y})/V_{\lambda,y}}{\sum_y P_{\lambda,y}^2/V_{\lambda,y}}, \quad (3)$$

where  $V_{\lambda,y}$  is the variance in each pixel calculated assuming Poisson noise,

$$V_{\lambda,y} = S_{\lambda,y} + B_{\lambda,y}. \quad (4)$$

The standard deviation of an optimally extracted spectral pixel is given by

$$\delta f_{\lambda}^{\text{opt}} = \left( \sum_y P_{\lambda,y}^2/V_{\lambda,y} \right)^{-1/2} \quad (5)$$

(Horne 1986). For our faint spectra, application of this technique resulted in an increase in the S/N of approximately 70% over the simpler extraction method discussed above. We will henceforth refer to each of the spectral data points from the optimal extraction as a ‘‘spectral pixel.’’

Figures 2a, 2b, and 2c show the optimally extracted flare 1, flare 2, decay, and quiescent count rate spectra in the SW, MW, and LW spectral regions. The spectral pixel resolutions are  $\sim 0.5$ , 1.0, and 2.0 Å, respectively. The S/N varies from near zero in the continuum to almost four in the strongest lines.

In Table 1 we identify the strongest lines in the 12 spectra in Figures 2a, 2b, and 2c and give the ion, the peak line formation temperature, the line count flux at Earth (or the upper limit), and the S/N if the line was detected. A Gaussian fitting routine was used to fit each potential line (Ayres 1993, and references therein). The peak wavelength was allowed to vary by  $\pm 1$  resolution element (i.e.,  $\pm 2$  spectral pixels) during the fit; the Gaussian width was also allowed to vary. The potential lines and wavelengths were chosen from the line list of Monsignori Fossi & Landini (1994b). Only lines with a S/N greater than  $2\sigma$  were considered as possible detections. The table shows 3  $\sigma$  upper limits for lines that do not meet this criteria. Some strong lines obviously not present in the spectra are included in Table 1 as upper limits to provide better coverage across the *EUVE* temperature-sensitivity range.

The FWHM of the Gaussian fit was also used as a selection criterion. Spurious emission features caused by MCP hot spots have FWHM much smaller than one resolution element; blended lines could be identified by their wide FWHM.

### 3. THE DIFFERENTIAL EMISSION MEASURE

In the ‘‘coronal approximation,’’ applicable in the corona and transition region of most active stars, emission is produced by collisional excitation followed by radiative decay in an optically thin plasma. The degree of ionization of an individual element in the plasma is a function of temperature, determined by a balance between collisional ionization and a combination of radiative and dielectronic recombination (see, e.g., Arnaud & Rothenflug 1985; Arnaud & Raymond 1992; Raymond 1995; Brickhouse, Raymond, & Smith 1995). The volumetric plasma emissivity at wavelength  $\lambda$  integrated over a single *EUVE* spec-

tral pixel can be written in the form  $n_e^2 G_{\lambda}(T)$ , where  $n_e$  is the electron density and  $G_{\lambda}(T)$  incorporates all the temperature-dependent atomic physics effects, such as ionization equilibrium curves and collisional rate coefficients. It also includes the assumed elemental abundances. In this paper, we adopt the line emissivities of Monsignori Fossi & Landini (1994b; computed in the ‘‘low-density’’ limit) and continuum emissivities from Gronenschild & Mewe (1978) for computing  $G_{\lambda}(T)$ .

The count-rate spectrum at each spectral pixel for a source observed at a distance  $d$  with an instrument with effective area  $A_{\text{eff}}(\lambda)$  through a hydrogen column  $N_{\text{H}}$  is then given by

$$f_{\lambda} = \frac{A_{\text{eff}}(\lambda)e^{-N_{\text{H}}\sigma(\lambda)}}{4\pi d^2} \int_V G_{\lambda}(T)n_e^2 dV, \quad (6)$$

where  $\sigma(\lambda)$  is the ISM-absorption cross section (Rumph, Bowyer, & Vennes 1994), and  $A_{\text{eff}}(\lambda)$  is taken from EGODATA 1.8.1. This equation can also be written as

$$f_{\lambda} = \frac{A_{\text{eff}}(\lambda)e^{-N_{\text{H}}\sigma(\lambda)}}{4\pi d^2 h\nu} \int G_{\lambda}(T)\xi(T)d\ln T, \quad (7)$$

where

$$\xi(T) \equiv n_e^2(T) \left| \frac{d\ln T}{dV} \right|^{-1}. \quad (8)$$

The quantity  $\xi(T)$  is known as the ‘‘differential emission measure’’ (or ‘‘DEM’’) and is a useful concept because it can be computed from theoretical models and thus allows for a comparison of theory with observation. This definition of the DEM is slightly different (and more general) than the standard definition, since it works with differential volume elements instead of the differential height elements frequently assumed when the emission is known to be close to the star.

For spectral pixels containing unblended emission lines,  $G_{\lambda}(T)$  is typically a peaked function of temperature that is approximately symmetric about the peak temperature  $T_{\text{max}}$  with an emissivity width  $\Delta \log T \simeq 0.3$  or  $\Delta \ln T \simeq 0.7$ . We denote the peak value  $G_{\lambda}(T_{\text{max}})$  as  $G_{\text{max}}$ . For the individual lines we have analyzed (see Table 1), we define  $\Delta \ln T$  as

$$\Delta \ln T \equiv \frac{\int G_{\lambda}(T)d\ln(T)}{G_{\text{max}}}. \quad (9)$$

These quantities can be used to obtain approximate solutions for the DEM. If we assume that contributions to the temperature integral in equation (7) are negligible outside the range  $\ln T_{\text{max}} - (\Delta \ln T)/2 < \ln T < \ln T_{\text{max}} + (\Delta \ln T)/2$ , the mean value theorem yields

$$f_{\lambda} = \frac{A_{\text{eff}}(\lambda)e^{-N_{\text{H}}\sigma(\lambda)}}{4\pi d^2 h\nu} \xi(T') \int G_{\lambda}(T)d\ln T \quad (10)$$

or

$$f_{\lambda} = \frac{A_{\text{eff}}(\lambda)e^{-N_{\text{H}}\sigma(\lambda)}}{4\pi d^2 h\nu} \xi(T')G_{\text{max}}\Delta \ln T, \quad (11)$$

where  $\xi$  is evaluated at an undetermined intermediate temperature  $T'$ . Since the range of temperature  $\Delta \ln T$  is small when compared to the entire range of temperatures sampled by all observed lines in the *EUVE* spectrum, we will assume  $T' = T_{\text{max}}$  in the course of plotting DEM values obtained in this fashion, but one must remember that the temperature corresponding to the DEM value is somewhat uncertain.

By using equation (11) to estimate  $\xi(T_{\max})$  for a sequence of lines whose values of  $T_{\max}$  span a wide temperature range, the variation of  $\xi(T)$  with  $T$  can be investigated. This procedure (the ‘‘Pottasch’’ method; see Pottasch 1963) was used to estimate the DEM values in Tables 2 and 3, as well as the individual solid points in the panels of Figure 5. However, the usefulness of this technique is limited. It fails

to work for strongly blended lines and does not take advantage of partial information available from the large number of marginally detected lines. In addition, the approximation is poor if the DEM is a strongly varying function of temperature or if the emissivity covers a very broad range of temperature (e.g., He-like ions) or has a strongly asymmetric temperature variation (e.g., Li-like ions). For these

TABLE 2  
DEM FOR INDIVIDUAL SPECTRAL LINES (SOLAR CORONAL ABUNDANCES)

Wavelength (Å)	Ion	$\log_{10} T$	$\Delta \ln T$	$\log_{10}$ Quiet DEM <sup>a</sup> (cm <sup>-3</sup> )	$\log_{10}$ Flare 1 DEM <sup>a</sup> (cm <sup>-3</sup> )	$\log_{10}$ Decay DEM <sup>a</sup> (cm <sup>-3</sup> )	$\log_{10}$ Flare 2 DEM <sup>a</sup> (cm <sup>-3</sup> )
584.4	He I	4.54	1.11	<51.7	<54.0	<53.9	<54.2
303.9	He II	4.91	0.80	<49.1 <sup>b</sup>	<50.1 <sup>b</sup>	<50.1 <sup>b</sup>	<50.4 <sup>b</sup>
554.4	O IV	5.28	0.68	<48.6	<50.5	<50.6	<51.0
238.5	O IV	5.34	0.56	<49.8	<50.2	<50.6	<50.8
358.9	Ne V	5.50	0.71	<49.4	<50.5	<50.6	<51.2
401.7	Ne VI	5.65	0.60	<49.2	<50.6	<50.8	<51.1
171.1	Fe IX/O V	5.85	0.83	<48.6	<48.9	<49.2	<49.4
177.2	Fe X	5.99	0.58	<49.9	<49.8	<50.1	<50.3
174.5	Fe X	5.99	0.58	<49.5	<49.5	<49.7	<50.6
180.6	Fe XI	6.07	0.53	<49.4	<50.4	<50.3	<50.9
202.1	Fe XIII	6.20	0.49	<49.3	<49.6	<49.9	<50.1
284.2	Fe XV	6.32	0.56	49.5	<50.0	<50.3	<50.6
335.4	Fe XVI	6.41	0.83	49.6	<50.4	<50.5	<50.8
93.3	Fe XVIII	6.81	0.71	50.3	50.8	50.8	<51.2
108.4	Fe XIX	6.89	0.61	50.5	50.9	50.7	<51.3
121.6	Fe XX	6.95	0.58	<50.4	51.0	<50.8	<51.3
118.7	Fe XX	6.95	0.58	<50.7	51.1	<51.1	<51.6
128.7	Fe XXI	7.02	0.57	50.2	51.0	50.5	<51.2
135.8	Fe XXII	7.08	0.61	50.6	51.1	<50.9	<51.5
116.3	Fe XXII	7.08	0.60	<50.7	<51.1	<51.1	<51.6
117.2	Fe XXII	7.08	0.61	50.6	51.3	<50.8	<51.3
132.8	Fe XXIII/XX	7.15	0.74	50.2	51.0	50.5	50.8 <sup>c</sup>
255.1	Fe XXIV	7.24	1.06	<50.8	<51.4	<51.6	<51.9
192.0	Fe XXIV/O V	7.24	1.06	<50.4	<50.8	<51.1	<51.3

<sup>a</sup> Eq. (11) was used to approximate DEM values.

<sup>b</sup> Line actually detected with listed S/N. Lower limit denoted caused by possible competing ionization mechanisms such as photoionization. See text.

<sup>c</sup> Small width may indicate spurious detection. See text.

TABLE 3  
DEM FOR INDIVIDUAL SPECTRAL LINES (0.1 × SOLAR CORONAL)

Wavelength (Å)	Ion	$\log_{10} T$	$\Delta \ln T$	$\log_{10}$ Quiet DEM <sup>a</sup> (cm <sup>-3</sup> )	$\log_{10}$ Flare 1 DEM <sup>a</sup> (cm <sup>-3</sup> )	$\log_{10}$ Decay DEM <sup>a</sup> (cm <sup>-3</sup> )	$\log_{10}$ Flare 2 DEM <sup>a</sup> (cm <sup>-3</sup> )
584.4	He I	4.54	1.11	<52.7	<55.0	<54.9	<55.2
303.9	He II	4.91	0.80	<50.1 <sup>b</sup>	<51.1 <sup>b</sup>	<51.1 <sup>b</sup>	<51.4 <sup>b</sup>
554.4	O IV	5.28	0.68	<48.6	<50.5	<50.6	<51.0
238.5	O IV	5.34	0.56	<49.8	<50.2	<50.6	<50.8
358.9	Ne V	5.50	0.71	<50.4	<51.5	<51.6	<52.2
401.7	Ne VI	5.65	0.60	<50.2	<51.6	<51.8	<52.1
171.1	Fe IX/O V	5.85	0.83	<49.6	<49.9	<50.2	<50.4
177.2	Fe X	5.99	0.58	<50.9	<50.8	<51.1	<51.3
174.5	Fe X	5.99	0.58	<50.5	<50.5	<50.7	<51.0
180.6	Fe XI	6.07	0.53	<50.4	<51.4	<51.3	<51.9
202.1	Fe XIII	6.20	0.49	<50.3	<50.6	<50.9	<51.1
284.2	Fe XV	6.32	0.56	50.5	<51.0	<51.3	<51.6
335.4	Fe XVI	6.41	0.83	50.6	<51.4	<51.6	<51.8
93.3	Fe XVIII	6.81	0.71	51.3	51.8	51.8	<52.2
108.4	Fe XIX	6.89	0.61	51.5	51.9	51.7	<52.3
121.6	Fe XX	6.95	0.58	<51.4	52.0	<51.8	<52.3
118.7	Fe XX	6.95	0.58	<51.7	52.1	<52.1	<52.6
128.7	Fe XXI	7.02	0.57	51.2	52.0	51.5	<52.2
135.8	Fe XXII	7.08	0.61	51.6	52.1	<51.9	<52.5
116.3	Fe XXII	7.08	0.60	<51.7	<52.1	<52.1	<52.6
117.2	Fe XXII	7.08	0.61	51.6	52.3	<51.8	<52.3
132.8	Fe XXIII/XX	7.15	0.74	51.2	52.0	51.5	51.8 <sup>c</sup>
255.1	Fe XXIV	7.24	1.06	<51.8	<52.4	<52.6	<52.9
192.0	Fe XXIV/O V	7.24	1.06	<51.4	<51.8	<52.1	<52.3

<sup>a</sup> Eq. (11) was used to approximate DEM values.

<sup>b</sup> Line actually detected with listed S/N. Lower limit denoted caused by possible competing ionization mechanisms such as photoionization. See text.

<sup>c</sup> Small width may indicate spurious detection. See text.

reasons, we supplement the Pottasch DEM points with the DEM determined from a regularized inversion procedure (see § 4).

#### 4. THE INVERSION METHOD

Equation (7) can be evaluated for every spectral pixel in our *EUVE* spectrum given  $\xi(T)$  since  $G_\lambda(T)$  can be found for each wavelength from the plasma emissivity code. The results can then be compared with the observed count spectrum  $f_\lambda$ . Our objective is to invert this problem and solve the series of Fredholm integral equations in equation (7) for  $\xi(T)$ , given  $G_\lambda(T)$  and  $f_\lambda$ .

Inversion problems of this type are notoriously difficult (Judge, Hubeny, & Brown 1997). We describe here the final approach we have taken; in the interest of space we provide only a limited discussion of why these steps were taken. Further details may be found in Cully (1997).

To find the DEM numerically, it is necessary to discretize the temperature space on which  $\xi(T)$  is defined. In this paper, the temperature is defined at increments of 0.1 in  $\log T$  (or 0.23 in  $\ln T$ ), varying from  $\log T = 5.0$  to  $\log T = 7.5$ . A logarithmic scale is chosen because the integration variable in equation (7) is  $\ln T$ , and this will convert the integral into a simple sum.  $\xi(T)$  is assumed to be a continuous, piecewise linear function between adjacent points in  $\log T$ . The spectra are already defined on a finite grid in wavelength  $\lambda$  (i.e., the spectral pixels; see § 2). If we denote the number of temperature points by  $N$  and the number of wavelength points by  $M$ , equation (7) evaluated at the observed wavelengths can be rewritten as the matrix equation

$$f_i = \sum_{j=1}^N K(\lambda_i, T_j) \xi_j \equiv \sum_{j=1}^N K_{i,j} \xi_j \quad \text{for } i = 1, M, \quad (12)$$

or in vector notation, as  $\mathbf{f} = \mathbf{K}\boldsymbol{\xi}$ .

Here,  $f_i$  is the count flux at  $\lambda_i$ ,  $\xi_j$  is the DEM at temperature  $T_j$ , and  $K_{i,j}$  is called the kernel function or kernel matrix. The piecewise linear assumption for  $\xi(T)$  results in  $K_{i,j}$  having the form

$$K_{i,j} = (A_{i,j} - B_{i,j})(1 - \delta_{j,N}) + B_{i,j-1}(1 - \delta_{1,j}), \quad (13)$$

where

$$A_{i,j} = \frac{A_{\text{eff}}(\lambda_i) e^{-N_H \sigma(\lambda_i)}}{h\nu 4\pi d^2} \int_{y_j}^{y_{j+1}} G_{\lambda_i}(y) dy, \quad (14)$$

and

$$B_{i,j} = \frac{A_{\text{eff}}(\lambda_i) e^{-N_H \sigma(\lambda_i)}}{h\nu 4\pi d^2} \frac{1}{\Delta y} \int_{y_j}^{y_{j+1}} (y - y_j) G_{\lambda_i}(y) dy. \quad (15)$$

The integration variable  $y$  is  $\ln T$ , and  $\Delta y$  is the spacing between temperature bins in  $\ln T$  ( $\Delta y = 0.2303$  here). We have found through experimentation that assuming  $\xi(T)$  to be continuous and piecewise linear improves the accuracy and stability of the equations over that obtained when  $\xi(T)$  is assumed to be piecewise constant (in the latter case there would be no  $B_{i,j}$  terms). Each column of the kernel matrix (variation in  $i$  for fixed  $j$ ) can be thought of as the theoretically computed spectrum from a nearly isothermal plasma with temperature  $T_j$  (the plasma temperature is actually distributed between  $T_{j-1}$  and  $T_{j+1}$ , but with most of the plasma near  $T_j$ ). The integrals in equations (14) and (15) are evaluated numerically.

The spectra in the SW, MW, and LW detectors of *EUVE* overlap slightly in wavelength; our approach is to assume

that each of the 3 datasets are statistically independent of one another; the spectra are placed end-to-end to form a single full spectrum. Because of the slight overlap, the wavelength  $\lambda_i$  is not strictly monotonic with its index  $i$ , but this presents no difficulties.

For the *EUVE* data, the solution to equation (12) is overdetermined ( $M \gg N$ ), meaning that a direct inversion for  $\xi_j$  is impossible. Our approach is to invert for  $\xi_j$  using "regularization" (Craig & Brown 1986; Mewe et al. 1995). In the regularization procedure, a best-fit  $\xi_j$  is found by minimizing the quantity  $\|\mathbf{K}\boldsymbol{\xi} - \mathbf{f}\|^2 + \Lambda \|\boldsymbol{\xi}'\|^2$ , where  $\|\mathbf{x}\|^2 \equiv \sum_k x_k^2$ , and  $\boldsymbol{\xi}' \equiv (\xi_{j+1} + \xi_{j-1} - 2\xi_j)/2\Delta y$ . Performing that minimization results in the equation

$$(\mathbf{K}^T \mathbf{K} + \Lambda \mathbf{H})\boldsymbol{\xi} = \mathbf{K}^T \mathbf{f}, \quad (16)$$

where  $\mathbf{K}^T$  is the transpose of  $\mathbf{K}$ ,  $\mathbf{H}$  is the banded "smoothing matrix" (eq. [6.12] of Craig & Brown 1986), and the scalar coefficient  $\Lambda$  is called the "smoothing parameter." Given a value of  $\Lambda$ , equation (16) can be solved for  $\xi_j$  using singular-value decomposition techniques (Press et al. 1992).

The role of  $\Lambda$  in equation (16) is to control unstable oscillations that result if no constraint is placed on the solution  $\xi_j$ . The particular constraint we have applied is to limit the magnitude of the second derivative of  $\xi$  with respect to  $\ln T$ . In the limit  $\Lambda \rightarrow 0$  (no smoothing), equation (16) reduces to the least-squares solution for  $\xi_j$ , which is mathematically ill-posed and unstable to errors in the measurements of  $f_i$  (Craig & Brown 1986). As  $\Lambda \rightarrow \infty$ , the solution is stable to random data errors but is always constrained to be a straight line. An important part of the inversion procedure (discussed further below) is to determine the optimal value of  $\Lambda$ , giving solutions that are stable but not oversmoothed and that exhibit physically meaningful variations of  $\xi$  with  $T$ .

Most of the *EUVE* spectral pixels in our data have low S/Ns. It was therefore necessary to revise the procedure outlined above in order to avoid the DEM solution being overwhelmed by the behavior of the many low S/N pixels. We introduce a weight  $w_i$  for each value of  $M$  in equation (16), where the weight depends on both data quality (i.e., the errors) and knowledge of the atomic physics [i.e.,  $G_\lambda(T)$ ]. An arbitrary weighting of each equation is made possible by the fact that for a given  $i$ , both  $f_i$  and the corresponding values of  $K_{i,j}$  can be multiplied by a factor  $w_i$  without affecting the basic equations (12). After performing this multiplication, however, the factor  $w_i$  does affect how much the solution for  $\xi$  from equation (16) is influenced by the spectrum at  $\lambda_i$ , with larger values of  $w_i$  giving the data  $f_i$  more importance in the inversion. After multiplication by  $w_i$ , we denote the weighted kernel matrix and its transpose by  $\tilde{\mathbf{K}}$  and  $\tilde{\mathbf{K}}^T$ , respectively, and the weighted data by  $\tilde{\mathbf{f}}$ . The final form of the inversion equation,  $(\tilde{\mathbf{K}}^T \tilde{\mathbf{K}} + \Lambda \mathbf{H})\boldsymbol{\xi} = \tilde{\mathbf{K}}^T \tilde{\mathbf{f}}$ , is identical (Craig & Brown 1986) to equation (16).

We adopt weights of the form

$$w_i = \frac{q_i}{\delta f_i}, \quad (17)$$

where  $\delta f_i$  is the estimated count error (eq. [5]), and  $q_i$  is given by

$$q_i = \frac{1}{\Gamma} \left[ \max_j \left( \frac{K_{i,j}}{\sum_k K_{k,j}} \right) \right]^\beta. \quad (18)$$

$\Gamma$  is determined by the normalization  $\sum_{i=1}^M q_i^2 = 1$ . If  $q_i$  were constant (see, e.g., Mewe et al. 1995), the weight  $1/\delta f_i$  in equation (17) would be similar to that in standard least-squares fits, in which  $\chi^2$  is minimized. Even if  $q_i$  varies, as in equation (18), the normalization factor  $\Gamma$  allows us to construct a minimization statistic that is analogous to  $\chi^2$ .

The quantity  $q_i$  requires further explanation. In most of the spectral pixels, the computed plasma emissivity  $G_\lambda(T)$  consists of either continuum emission only or of weak lines plus continuum. If  $q_i$  is constant, spurious noise contributions in these pixels are treated as being caused by continuum emission, and the inversion process therefore results in spuriously large DEM values at the high temperatures ( $\log T \gtrsim 7.3$ ) at which the EUVE continuum is produced most effectively. This problem is exacerbated by the wavelength dependence of continuum emission in the EUVE wavelength region being insensitive to temperature, although the level of the emission is strongly temperature dependent (Schrijver et al. 1995). This results in an ambiguity to the DEM distribution for  $\log T \gtrsim 7.3$ . We found that weighting by  $1/\delta f_i$  alone is not sufficient to suppress the contribution of noisy spectral pixels to the continuum, since there are so many of them. Furthermore, it is likely that our data contain spectral lines that are not yet included in the plasma emission code; these lines will also be treated as continuum emission by the inversion procedure. On the other hand, it is very significant if we see little or no emission at a wavelength corresponding to a strong line in the EUVE wavelength range, so data at that wavelength should be weighted accordingly. After much experimentation, we have found that the form of  $q_i$  given in equation (18) solves most of these problems. Figure 3 illustrates the behavior of  $q_i$  for the two choices  $\beta = 1.0$  and  $\beta = 0.5$ . As can be seen in the figure, equation (18) results in large weights at those wavelengths where strong lines are formed or could be formed. Continuum wavelengths are given low (though not zero) weighting. The relative weights between the strongest lines and the continuum (or weaker lines) can be controlled through the parameter  $\beta$ . As  $\beta \rightarrow \infty$ , the spectral pixel with the strongest emissivity goes to unit weight, and  $q_i$  at all other pixels goes to zero. For  $\beta = 0$ , all spectral pixels are given equal weight. For the inversions presented in this paper,  $\beta = 1.0$ .

Once this weighting scheme is introduced and a suitable value of  $\Lambda$  is chosen, it is possible to estimate the error  $\delta \xi_j$  in the solution. We perform a series of Monte Carlo simulations in which  $N'$  realizations of perturbed data are inverted to yield  $N'$  solutions  $\xi$ . The value of  $\Lambda$  is assumed to be fixed for all  $N'$  solutions (for the AD Leo inversions described in § 6, we choose  $N' = 1000$ ). Each realization of the data consists of adding a normally distributed random error with amplitude  $\delta f_i$  (eq. [5]) to each data value  $f_i$ . Errors at each data point are assumed to be uncorrelated with those at other data points. After a set of  $N'$  solutions has been computed, we estimate the error in  $\xi_j$  as

$$(\delta \xi_j)^2 = \overline{(\xi_j - \bar{\xi}_j)^2} + \Upsilon_j. \quad (19)$$

Here the overbar denotes ensemble average; thus  $\bar{\xi}_j$  is the mean solution, and the first term of equation (19) represents the variance about the mean and reflects the sensitivity of the inversion method to instabilities that vary with different incarnations of the data. The term  $\Upsilon_j$  represents an error caused by oscillations in the solution that do not vary with different incarnations of the data; it is estimated by inver-

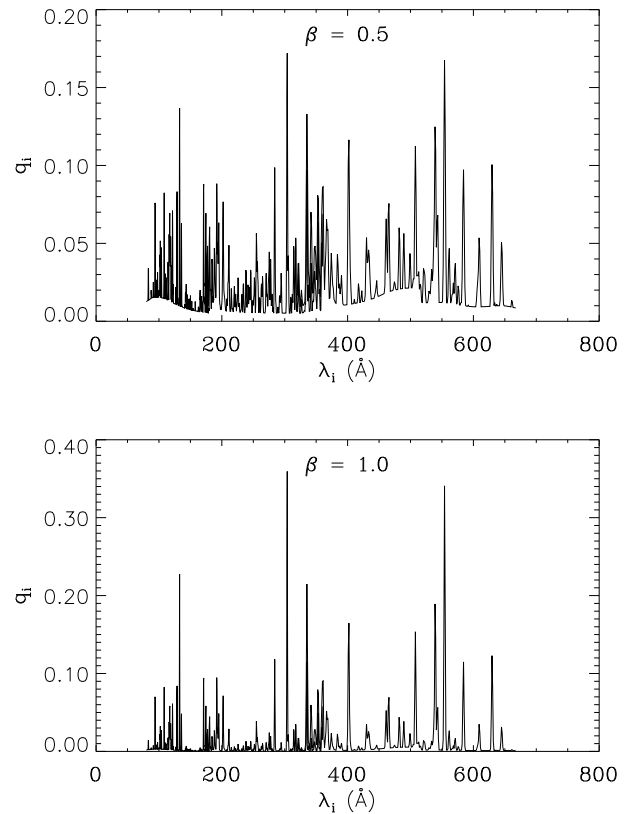


FIG. 3.—Weighting function  $q_i$  as a function of  $\lambda_i$  for the spectral pixels used in our inversion. Plots of both  $\beta = 0.5$  and  $\beta = 1.0$  are shown. The weights are strong where strong lines are or could be present and are weak in the continuum.  $\beta = 1.0$  was adopted for the inversion of the AD Leo data described in § 6.

ting spectra computed from an initially flat DEM using the same value of  $\Lambda$ . A complete discussion of how  $\Upsilon_j$  is determined can be found in Cully (1997); here we simply note that this term is important at small values of  $\Lambda$  and in temperature ranges without significant line contributions but is less important at optimal or large values of  $\Lambda$ .

We invested considerable effort in developing automatic and objective algorithms for finding the best smoothing parameter  $\Lambda$ , especially the “statistical regularization” approach (Craig & Brown 1986) and variations on that technique. Eventually, we concluded that the most reliable method was simply to compute a sequence of inverted DEM curves (and the associated error curves) for a wide range of  $\Lambda$  values and to then choose the smallest value of  $\Lambda$  for which the solutions show no obvious sign of unstable oscillations or significant negative excursions. We also use the Pottasch points and the upper limits (§ 3) as a rough guide for choosing  $\Lambda$ ; we expect the DEM distribution to be a smooth function that passes through or near these points. In § 5, we illustrate this inversion procedure for a simulated dataset with an adopted DEM, showing the effects of the S/N and the choice of smoothing parameter on the solutions.

Finally, once a value of  $\Lambda$  has been selected, it is possible (in principle) to determine “best-fit” values for  $N_H$  and/or values of the iron abundance,  $[\text{Fe}/\text{H}]$ , by comparing the observed spectrum to the spectrum computed from the DEM (for  $[\text{Fe}/\text{H}]$  variations,  $G_\lambda(T)$  must be recomputed for each value of  $[\text{Fe}/\text{H}]$ .) By varying  $N_H$  and  $[\text{Fe}/\text{H}]$ , one can attempt to minimize the  $\chi^2$  of the fit between the observed

and model spectra. As discussed in § 6, we were able to find a best-fit value for  $N_{\text{H}}$ , but the value of  $[\text{Fe}/\text{H}]$  was not constrained by our data.

### 5. INVERSION OF SIMULATED DATA

To verify and understand the performance of our inversion scheme, we tested the above method with simulated data produced using an adopted test DEM. The kernel matrix was computed using the formalism described in § 4 with solar coronal values for the abundances (Feldman 1992; see also § 6) used in  $G_{\lambda}(T)$ . The value of  $A_{\text{eff}}(\lambda)$  and the resolution of the spectrometers are taken from EGODATA 1.8.1. The distance  $d$  was taken to be 4.9 pc, and  $N_{\text{H}} = 2 \times 10^{18} \text{ cm}^{-2}$ . Spectra were computed separately from equation (12) for the SW, MW, and LW spectrometers and then placed end-to-end to form a single full spectrum, as described in § 4.

For our test DEM, we set  $\xi_j$  to a sine wave with maxima at  $\log T = 5$ ,  $\log T = 6$ , and  $\log T = 7$  (the solid curve in Fig. 4). The sine wave is offset such that the minimum value is zero, and the maximum value is 1000 in arbitrary units. This test DEM was chosen because it presents a challenge for the regularization method, which tends to find straight lines if  $\Lambda$  is too large. Synthetic spectra were first computed as in equation (12), and a background noise component was then added to simulate the effects of the detector background on the spectrum. This noise level was controlled

such that the S/N of the strongest line in the spectrum was equal to the value given at the top of each of the panels of Figure 4 (29 and 3, respectively).

The simulated spectra were analyzed using the same procedure as for the actual data (§ 6). First, we removed from consideration the spectral pixels near the detector edges and within one resolution element of the strongest helium lines (237, 243, 256, 304, and 584 Å) in both the spectra  $f_i$  and in  $K_{i,j}$ . Although the helium lines provide strong constraints on the DEM curve at low temperatures ( $\log T < 5.0$ ), we chose not to include them since they can have higher count rates than expected by pure electron-collision-dominated excitation (Feldman 1992, and references therein). If these lines were included, they could bias the solution to artificially high values at low temperatures.

We performed a sequence of Monte Carlo simulations as described in § 4 for each value of  $\Lambda$  considered, spanning the range from  $\Lambda = 10^{-14}$  to  $\Lambda = 10^{-3.5}$ . The amplitude of the errors was estimated from the given S/N, as determined from the computed spectrum plus the background. We performed  $N' = 100$  simulated inversions for each value of  $\Lambda$ . The resulting average DEM from the inversions (*dashed curve*) is shown in Figure 4 for several values of  $\Lambda$ . The estimated errors computed from equation (19) are shown by the dotted curves that surround each dashed curve.

Figure 4 illustrates several important properties of the inversion method. For very small values of  $\Lambda$ , the individual

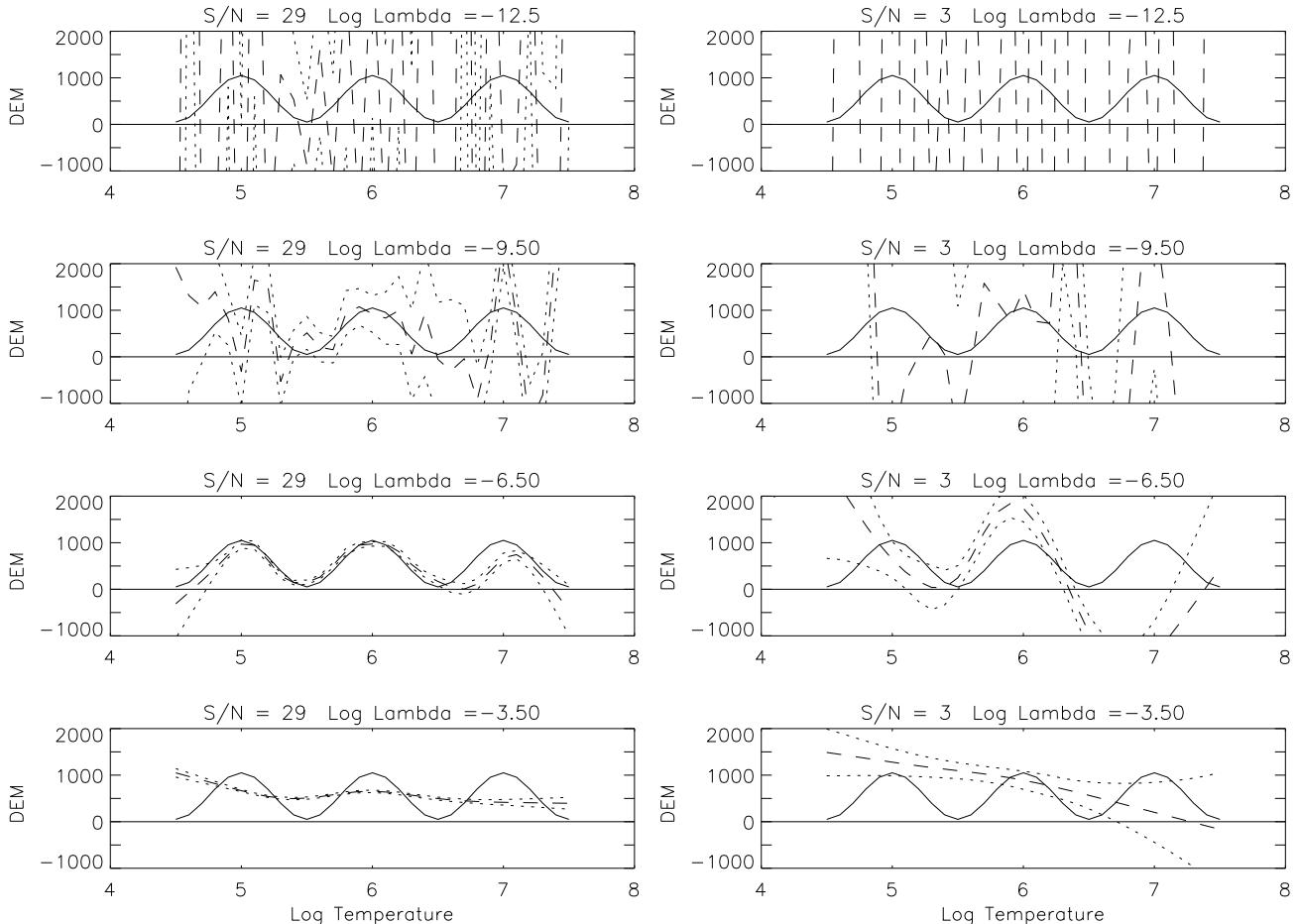


FIG. 4.—Calculated DEM curves computed from simulated spectra assuming a given test DEM curve (*solid line*) and a given signal-to-noise ratio (S/N = 29 in the left-hand panels, and S/N = 3 in the right-hand panels) for a range of smoothing parameters ( $\Lambda$ ), as discussed in § 5. DEM is in arbitrary units.

solutions are highly unstable, as evidenced by the large calculated errors in  $\xi_j$ . This produces  $\xi_j$  solutions that also contain large oscillations. As the value of  $\Lambda$  increases, the maximum allowed value of the second derivative decreases, the oscillations are increasingly damped, and the DEM solutions more closely match the test DEM. As  $\Lambda$  increases further, the maximum second derivative allowed in the solution becomes smaller than the second derivatives of the test DEM, resulting in an oversmoothed solution. The errors in the inversion solution produced by oversmoothing are unfortunately not reflected in the error computed by equation (19). Instead, the computed error envelope continues to decrease with increasing  $\Lambda$  because of the smoothing effect of  $\Lambda$  on the individual DEM solutions in the Monte Carlo Method. As described in § 4, we found that the best choice of  $\Lambda$  is determined by a compromise between excessive oscillation and oversmoothing.

We can also see the effect of S/N on the solution behavior. Equation (17) for the weights  $w_i$  used in  $\tilde{K}$  and  $\tilde{f}$  show that, in general, data with smaller errors are weighted more heavily relative to the smoothing term  $\Lambda H$  in equation (16). Thus the ratio between  $\tilde{K}^T \tilde{K}$  and  $\Lambda H$  increases with higher S/N for a given value of  $\Lambda$ . This has the same effect as reducing  $\Lambda$  with the S/N held constant. Thus, as errors in the data are reduced, less smoothing is required.

The same effect can also be seen in different parts of a given DEM solution. If the plasma spectrum at a given temperature contains a large number of lines, or a few strong lines, the solution near that temperature will be constrained more than other parts of the solution because of stronger weighting (eq. [18]). Conversely, for temperatures at which few lines are present, the solutions are less constrained. Since the method is designed to limit the second derivative of the solution, a constant second derivative is found in areas where there is little constraint on the data from strong lines, as in  $\log T \lesssim 5.0$  and  $\log T \gtrsim 7.2$ . Solutions beyond these limits should be considered suspect, as indicated by the divergence in the error curves. At temperatures where there are no strong lines in the spectrum (such as near  $\log T = 6.7$  in Fig. 4), the solution can also deviate significantly outside the error curves from the test DEM.

## 6. RESULTS FROM AD LEO DATA

As noted in § 4, the hydrogen column density  $N_H$ , the iron abundance  $[\text{Fe}/\text{H}]$ , and the differential emission measure (DEM) as a function of temperature can, in principle, be determined simultaneously from the observed spectra. After a great deal of effort (and much experimentation with the weighting parameter  $\beta$  in eq. [18]), we have concluded that, in practice, the iron abundance is essentially unconstrained by our data. To obtain a good estimate of  $[\text{Fe}/\text{H}]$ , both Fe and H must be measured from plasma at nearly the same temperature (otherwise changes in abundance mimic changes in the DEM). Hydrogen, through thermal bremsstrahlung, does contribute significantly to the continuum radiation in the short-wavelength portion of the EUVE SW spectrum where several strong iron lines are also formed at  $T > 10^7$  K. Unfortunately, the S/N of our data is very low in the continuum, and we cannot claim a positive detection of continuum radiation. We therefore decided to investigate two assumed values of  $[\text{Fe}/\text{H}]$ , the solar coronal abundance and a value of 1/10 that. These bracket the solar photospheric abundance because of the first ionization potential

(FIP) effect in the solar corona (Meyer 1991), which gives a value for the coronal abundance that is  $\sim 3$  times the photospheric abundance. Using solar coronal abundance values assumes that the FIP effect operates in dMe stars as it does on the Sun; we regard this as an unproven but reasonable assumption. We prefer the solar coronal abundance value since AD Leo is thought to be a member of the young disk population and should thus have at least solar, if not greater, metallicity. However, the possible existence of the metal abundance deficiency syndrome (Drake, Laming, & Widing 1996; Schmitt et al. 1996) influenced us to investigate the 1/10 solar coronal abundance value also. Since the most important emission lines in the EUVE wavelength range are from iron, reducing  $[\text{Fe}/\text{H}]$  also reduces  $G_\lambda(T)$ , which requires a corresponding increase in the DEM to give a spectral line of the observed strength. Thus, the effect of reducing  $[\text{Fe}/\text{H}]$  by a factor of 10 is to increase the DEM by a factor of 10 (for those regions where iron-line radiation dominates the spectrum).

In contrast to the abundance determination, the hydrogen column density  $N_H$  was constrained by our data. Emission lines from neon, oxygen, and iron span the SW, MW, and LW regions of the spectrum. Photons emitted in these lines are preferentially absorbed at long wavelengths in the Lyman continuum by the intervening neutral hydrogen column between AD Leo and the EUVE detector. The DEM was computed for a range of  $N_H$  values, and the resulting synthetic spectra compared to the observed spectra. Minima in the  $\chi^2$  of the fit for each time period were found; combining the four results formally yields  $N_H = (2.65 \pm 0.83) \times 10^{18} \text{ cm}^{-2}$ . Including only the most significant digits, this is  $N_H = (3 \pm 1) \times 10^{18} \text{ cm}^{-2}$ . The value of  $N_H$  is insensitive to the assumed metal abundance since it is the ratio of line strengths of the same element in the long-, medium-, and short-wavelength regions that determines the required hydrogen column. This ratio is unaffected by changes in the abundance but strongly affected by the wavelength dependence of the Lyman continuum absorption. We note that the inversion method allowed us to use the information contained in weak and blended lines to find  $N_H$  unambiguously; this represents a significant advantage over the Pottasch method.

Using the two assumed  $[\text{Fe}/\text{H}]$  values and  $N_H = 3 \times 10^{18} \text{ cm}^{-2}$ , we then determined the DEM distribution as a function of temperature for the AD Leo spectra during the four time periods described in § 2 (Fig. 1). We used both the Pottasch method (§ 3) and the inversion method (§ 4) to compute the DEM. The results for the solar coronal abundance are shown in Figure 5 for the following periods: quiescent, flare 1, decay, and flare 2 (hereafter referred to as Q, F1, D, and F2). Figure 5 is presented in the usual log DEM versus log  $T$  format. The Pottasch results for the strong lines are shown as solid squares and the upper limits for weaker lines are shown as downward-pointing arrows. The solid curve gives the inversion results—note that the log-log format causes dropouts when the DEM becomes small. In fact, the DEM found from the inversion analysis is a smooth curve and is more naturally presented in a log-linear plot, as in Figure 6. The dotted lines in Figure 5 represent the estimated error of the inverted DEM (see § 4).

The Pottasch and inversion DEM results are in good agreement. Neither method gives a clearly superior result for these noisy data. Our expectation from § 5 is that the inversion method will prove superior if the data have higher

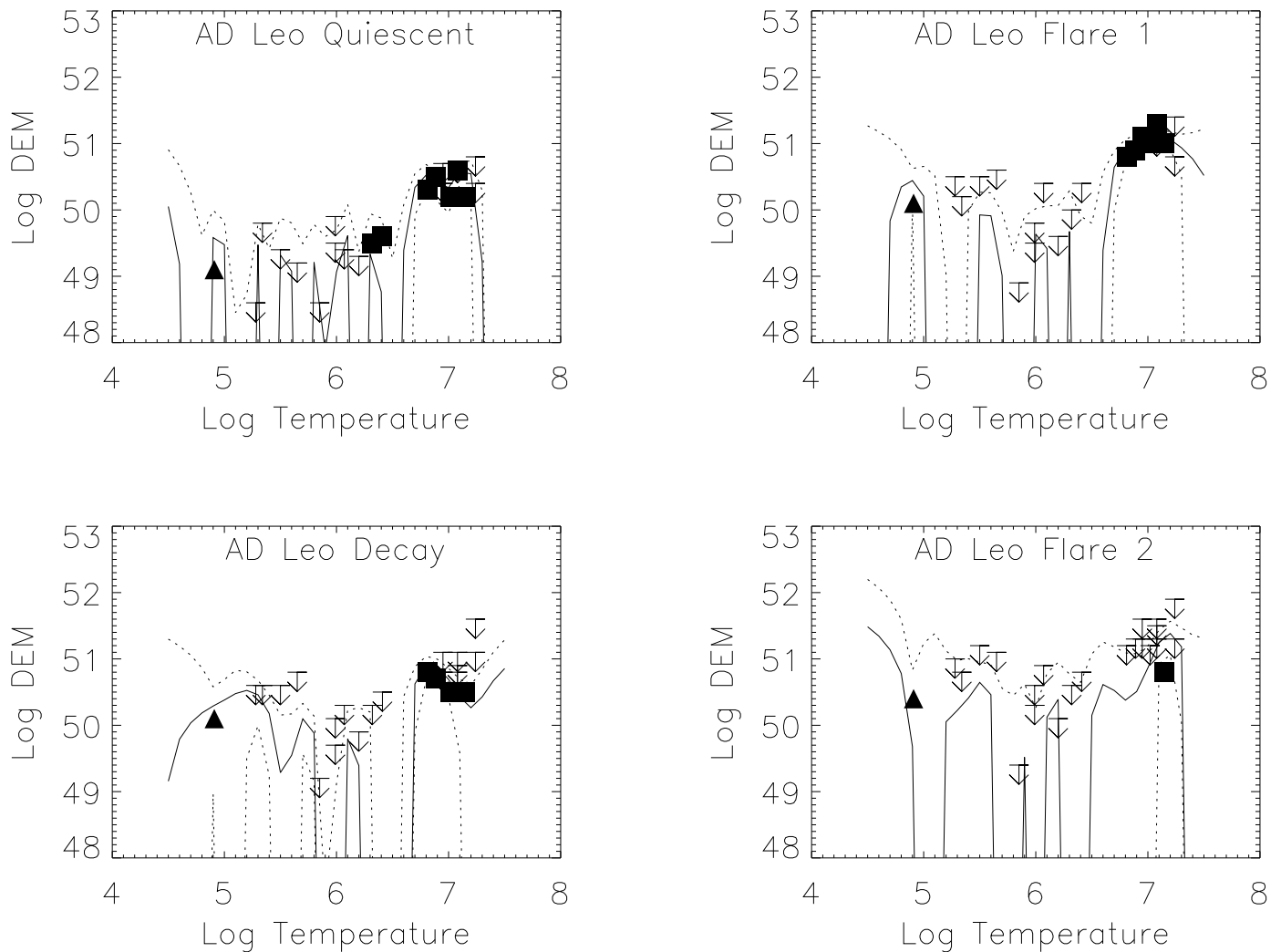


FIG. 5.—Results of the inversion analysis for the quiescent, flare 1, decay, and flare 2 spectra assuming solar coronal abundances. The Pottasch points calculated from the single lines listed in Tables 2 and 3 are shown as solid squares or upper limits. The triangle represents the emission from He II  $\lambda 304$  and should be considered an upper limit because of possible competing effects such as photoionization. The case of 0.1 times solar coronal [Fe/H] (not shown here) has DEM distributions roughly 10 times larger than these.

S/N, particularly if many lines are detected but blended. Decreasing the value of  $\beta$  in equation (18) also gives the option of weighting the continuum more heavily, e.g., to attempt to determine the metal abundance as described in § 4. For the present investigation, we simply adopt a DEM that is consistent with the results from both methods.

The quiescent data had the highest S/N and the largest number of positively detected lines (because of the period's long cumulative integration time). From the quiescent DEM, we identify the temperature regime between  $\sim 10^6$  and  $10^{7.2}$  K as the part of the DEM that can usefully be analyzed for the AD Leo data. We do have a detection of the He II line at  $304 \text{ \AA}$  that is formed near  $10^5$  K. However, the lack of other lines in the *EUVE* wavelength region that are formed at temperatures between  $10^5$  and  $10^6$  K, plus the ambiguity in the emission mechanism for the  $304 \text{ \AA}$  line, makes the DEM below  $10^6$  K very uncertain, so we will not discuss it further.

The basic shape of the DEM is similar for the four time periods. Figure 5 shows that there is a broad peak around temperatures of  $10^{6.8}$ – $10^{7.2}$  K with DEM of order  $10^{51}$   $\text{cm}^{-3}$  and a narrower detection around  $10^{6.2}$ – $10^{6.3}$  K with

DEM  $\sim 10^{49.5}$   $\text{cm}^{-3}$ . The lower temperature emission is only detected at a significant confidence level in the quiescent data, since it had the highest S/N. The higher temperature peak shows two interesting features. The temperature of the peak DEM varies from a maximum value of  $10^{7.2}$  K during F2 to a value of  $10^{7.1}$  K during F1 to a lower value of  $10^{6.8}$  K during D. Q indicates a flat plateau or possibly a double-peaked DEM distribution as determined from the strong lines formed between  $10^{6.8}$  and  $10^{7.2}$  K (Fig. 5) while the DEM determined from the inversion procedure indicates a broad distribution from a wide range of temperature ( $10^{6.6}$  to  $10^{7.2}$  K; see Fig. 6). The width of this plateau (0.4–0.6 in  $\log T$ ) is significantly greater than the emissivity width of the individual strong lines ( $\sim 0.3$  in  $\log T$ ). Evidently flare emission is concentrated at the highest temperatures and the decay emission at somewhat lower temperatures, with the quiescent emission coming from plasma spanning a broad range of temperatures.

Figures 5 and 6 also show that there is real structure in the high-temperature component during the F1 and D phases, with F1 showing a monotonic increase in the DEM

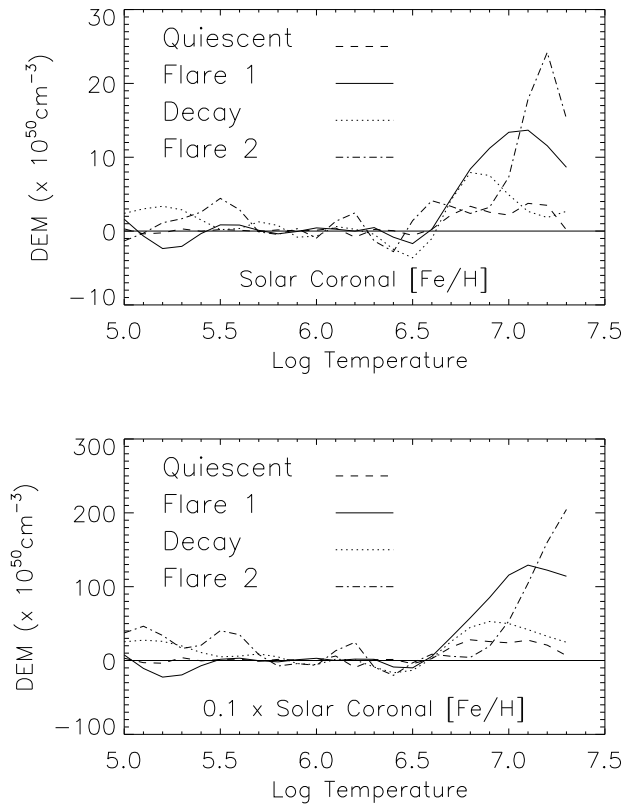


FIG. 6.—Results of the inversion analysis for the quiescent, flare 1, decay, and flare 2 spectra assuming solar coronal (*top panel*) and 0.1 times solar coronal abundances (*bottom panel*) plotted on a log-linear scale, which is the natural scale for the inversion method.

toward higher temperature and D showing a decrease in the DEM toward higher temperature.

## 7. DISCUSSION

Our results can be used to address the properties of the coronal loop structures on AD Leo and of the loop evolution during flares. First, we compare our results with a recent determination of the coronal emission measure for AD Leo. Second, we combine the formalism of Paper I with the temperature results from this paper to compute the loop sizes required to explain the observed flare evolution. We then compare these results to recent solar studies. Finally, we examine the difference in the DEM structure between the flare, decay, and quiescent phases and comment on the implications for coronal structure.

### 7.1. Comparison with Previous Work

An extensive analysis of the coronal emission measures of dMe stars, including AD Leo, has been carried out by G96. Their results differ from ours in several ways: they find a larger interstellar hydrogen column, very low metallicity, and larger emission measures in both the hot and cool components of their two-temperature fits. Their value for  $N_H$  is an order of magnitude larger than ours and is not supported by measures of the nearby (e.g.,  $\alpha$  Leo) ISM (Fruscione et al. 1994). Their metal-abundance estimate is one-tenth of the solar photospheric value, which is one-third of the smallest abundance we considered. The dis-

agreement that we find with their emission-measure (EM) values arises from these discrepancies. Both the larger hydrogen column and the lower metal abundance of G96 act to increase the amount of stellar emission required to produce the observed flux at earth and act to enhance the ratio of emission measure at low temperature ( $\sim 3 \times 10^6$  K) to that at high temperature ( $\sim 10^7$  K).

Another observational result of the G96 paper is that their high-temperature component appears to vary with time (possibly because of microflaring) while their low-temperature component remains steady. We find that, during flares, the EM at high temperature rises sharply, while the low temperature EM stays nearly constant. Thus, we concur with G96 that the time-varying (flare) activity occurs primarily at high temperature.

### 7.2. Loop Structure

In § 4.1 of Paper I, we showed how the temporal behavior of the EUVE DS light curve, in particular the rise and decay timescales (along with an estimate of the plasma temperature at the flare peak) could be used to derive such parameters as the loop length, the plasma pressure, and the coronal column depth at flare peak. In § 4.4 of Paper I, we compared estimates of plasma densities and loop lengths obtained in this fashion with those obtained using the traditional method of equating the observed decay time with the plasma cooling time to get the plasma density and hence the volume and estimates of the size of the loop. The two methods were found to agree to within factors of 2 or 3. The technique we developed in Paper I has the advantage that absolute fluxes need not be known and that no assumptions need be made about the loop aspect ratio to derive the loop length. We now have a better estimate of the flare loop apex temperature than was available to us in Paper I (for flare 1, we used  $T_A \simeq 2.5 \times 10^7$  K in Paper I; cf. the value found here of  $T_A \simeq 1.3 \times 10^7$  K), so we can recompute the loop parameters using the formalism presented there but with our new temperature results. Equations (4.10), (4.5), and (4.4) of Paper I show that  $L \sim T_A^{1/2}$ ,  $N_{\max} \sim T_A^2$ , and  $P_{\max} \sim T_A^{5/2}$ , where  $L$  is the loop length,  $N_{\max}$  is the peak coronal loop column depth achieved during the flare, and  $P_{\max}$  the corresponding peak loop pressure. If we were to retain the solar photospheric metallicity assumed in Paper I, these temperature scalings show that for F1, for example (where the peak temperature is somewhat less than our estimate in Paper I), the loop length would decrease slightly, the loop density and pressure would decrease more significantly, and the loop cross-sectional area coverage would increase.

The revised loop parameters shown in Tables 4 and 5 depend not only on the new  $T_A$  values but also on the assumed metallicity  $z$  of the plasma. (For the purposes of this discussion, we will assume that  $[\text{Fe}/\text{H}]$  and the overall metallicity  $z$  [the relative abundance of all metals to hydrogen, measured relative to the solar photospheric value] scale together. Thus for the solar coronal abundance case, we take  $z = 3.16$  and for the 0.1 times solar abundance case, we assume  $z = 0.316$ . Solar photospheric abundances would correspond to  $z = 1.0$ .) The combined effect of the  $T_A$  and  $z$  changes give (for the solar coronal value of  $z$ ) a longer loop but decreased values of  $P_{\max}$  and  $N_{\max}$ . The effect of changing the metallicity on the loop parameters can be seen by comparing the values obtained for our two assumed metallicities, i.e., those in Table 4 (solar coronal abundance)

TABLE 4  
CALCULATED LOOP PARAMETERS (SOLAR CORONAL)

Parameter	Flare 1	Flare 2
$T_A$ (K) .....	$13 \times 10^6$	$16 \times 10^6$
$L$ (cm) .....	$4.7 \times 10^{10}$	$2.4 \times 10^{10}$
$N_{\max}$ (cm $^{-2}$ ) .....	$1.9 \times 10^{20}$	$3.6 \times 10^{20}$
$n_{\max}$ (cm $^{-3}$ ) <sup>a</sup> .....	$4.0 \times 10^9$	$15 \times 10^9$
$P_{\max}$ (dyn cm $^{-2}$ ) .....	10	49
$B_{\text{Eq}}$ (G) <sup>b</sup> .....	16	35
$A_{\text{Cor}}$ (cm $^2$ ) <sup>c</sup> .....	$1.2 \times 10^{21}$	$1.5 \times 10^{20}$
$f$ (%) <sup>d</sup> .....	22	2.8
$V$ (cm $^3$ ) <sup>e</sup> .....	$1.1 \times 10^{32}$	$6.9 \times 10^{30}$
$E_{\text{th}}$ (ergs) <sup>f</sup> .....	$1.8 \times 10^{33}$	$5.1 \times 10^{32}$
$\log_{10} \text{EM}_{\max}$ (cm $^{-3}$ ) <sup>g</sup> .....	51.3	51.2

<sup>a</sup>  $N_{\max}/L$ .

<sup>b</sup>  $B_{\text{eq}} = (8\pi P_{\max})^{1/2}$ .

<sup>c</sup> Area of a single coronal loop footprint.

<sup>d</sup>  $f = 2A_{\text{cor}}/(4\pi R_{\odot}^2)$ .

<sup>e</sup>  $V = 2A_{\text{cor}}L$ .

<sup>f</sup>  $E_{\text{th}} = 1.5P_{\max}V$ .

<sup>g</sup>  $\text{EM}_{\max} = n_{\max}^2V$ .

and Table 5 (1/10 the solar coronal abundance). We can understand the  $z$ -dependence by noting that metal-line emission (primarily, though not entirely, from Fe) dominates the radiative loss function for temperatures between  $10^6$  and  $10^{7.2}$  K. Hence, changes in the metallicity will strongly influence the radiative loss rate, which in turn will influence the derived loop parameters. The radiative loss function  $\Phi(T)$  between  $10^6$  and  $10^{7.2}$  K can be approximated by the power-law relation  $\Phi(T) \sim AT^\alpha$ . Using metallicity-dependent fits to the Raymond-Smith (Raymond & Smith 1977) cooling curves from the Appendix of G96, we find the power-law index  $\alpha$  remains essentially unchanged with  $z$ , but the coefficient  $A \sim z$  (since the radiative losses scale as the number of emitters [i.e., the metal abundance] as long as the plasma is optically thin). Again using equations (4.10), (4.5), and (4.4) from Paper I, we find that  $L \sim z^{1/2}$ ,  $N_{\max} \sim z^{-1/2}$ , and  $P_{\max} \sim z^{-1}$ . The mean electron density in the loop is  $n_{\max} \sim N_{\max}/L \sim z^{-1}$ . Thus, for a fixed flux observed at earth, loops with smaller  $z$  will have shorter loop lengths, higher pressures, and higher densities.

TABLE 5  
CALCULATED LOOP PARAMETERS (0.1  $\times$  SOLAR CORONAL)

Parameter	Flare 1	Flare 2
$T_A$ (K) .....	$13 \times 10^6$	$<32 \times 10^6$
$L$ (cm) .....	$1.5 \times 10^{10}$	$1.1 \times 10^{10}$
$N_{\max}$ (cm $^{-2}$ ) .....	$5.9 \times 10^{20}$	$4.6 \times 10^{21}$
$n_{\max}$ (cm $^{-3}$ ) <sup>a</sup> .....	$4.0 \times 10^{10}$	$4.4 \times 10^{11}$
$P_{\max}$ (dyn cm $^{-2}$ ) .....	100	2800
$B_{\text{Eq}}$ (G) <sup>b</sup> .....	50	265
$A_{\text{Cor}}$ (cm $^2$ ) <sup>c</sup> .....	$4.1 \times 10^{20}$	$5.4 \times 10^{18}$
$f$ (%) <sup>d</sup> .....	7.8	0.10
$V$ (cm $^3$ ) <sup>e</sup> .....	$1.2 \times 10^{31}$	$1.1 \times 10^{29}$
$E_{\text{th}}$ (ergs) <sup>f</sup> .....	$1.9 \times 10^{33}$	$4.8 \times 10^{32}$
$\log_{10} \text{EM}_{\max}$ (cm $^{-3}$ ) <sup>g</sup> .....	52.3	52.3

<sup>a</sup>  $N_{\max}/L$ .

<sup>b</sup>  $B_{\text{eq}} = (8\pi P_{\max})^{1/2}$ .

<sup>c</sup> Area of a single coronal loop footprint.

<sup>d</sup>  $f = 2A_{\text{cor}}/(4\pi R_{\odot}^2)$ .

<sup>e</sup>  $V = 2A_{\text{cor}}L$ .

<sup>f</sup>  $E_{\text{th}} = 1.5P_{\max}V$ .

<sup>g</sup>  $\text{EM}_{\max} = n_{\max}^2V$ .

To estimate the change in the fractional area coverage with metallicity, we use the rise and decay timescales obtained from the *EUVE* Lex/B Deep Survey light curve as reported in Paper I and note that iron lines formed in this temperature range dominate the count rates observed between 40 and 190 Å over which the Deep Survey instrument is sensitive. If the observed count rate during the flares is to remain fixed, then  $A \times EM = A \times n_{\max}^2 LA_{\text{cor}} = \text{constant}$ , where  $A_{\text{cor}}$  is the mean cross-sectional area of the coronal loop. Using the relations shown above, we find  $A_{\text{cor}} \sim z^{1/2}$  and the loop volume  $V \sim LA_{\text{cor}} \sim z$ . Evidently loops with lower metal abundance are thinner and occupy less volume. A final interesting result is that the estimate of the peak thermal energy contained in the loop plasma,  $E_{\text{th}} = (3/2)P_{\max}V$ , is *independent* of the assumed metal abundance.

One must be cautious not to use these  $z$ -scaling results outside their ranges of validity. We assumed that the overall metallicity scales with the Fe abundance, but it is possible that stars with low Fe abundance may have normal abundances of other metals. We find that the radiative cooling curves computed with different values of [Fe/H] (but with other metal abundances held fixed) result in modest changes to the slope  $\alpha$  of the cooling curve, as well as a deviation (in the low  $z$  limit) from the  $A \sim z$  behavior noted above. Further, when the value of  $z$  drops below the range we consider in this paper, thermal bremsstrahlung losses (independent of  $z$ ) become important for  $T \gtrsim 10^7$  K.

The loop parameters given in Tables 4 and 5 have been computed from spectra that include both flaring and quiescent contributions; in principle, the quiescent spectra should be subtracted from the flare spectra before such an analysis is done. For these data, the low S/N makes this exercise impractical. We nevertheless believe that the quiescent emission does not have a significant impact on the derived loop quantities since the observed count rates for the highest temperature lines are much higher during flares than during quiescence. It is the highest temperature emission that determines the flare loop parameters.

For the AD Leo flares, the loop lengths that we obtain using either abundance are in excess of  $10^{10}$  cm. If we compare our loop parameters to those found for the high-temperature component of G96 (see their Fig. 3b), we find good agreement. Pressures of order  $10$  dyn cm $^{-2}$ , lengths of order a few  $\times 10^{10}$  cm, and filling factors of order 0.1 are required to fit their data; we find similar values by scaling the results of Tables 4 and 5 to their assumed metal abundance. As described in Paper I, it is the long rise and decay times observed for our flares that demand long loops. A recent paper shows that this is also true on the Sun. Metcalf & Fisher (1996) show that observed flare loop lengths are correlated with rise and decay timescales and loop temperatures in a very similar fashion to that described in Paper I. Some of the solar flare loops reach sizes of  $\sim 10^{10}$  cm, and these loops are consistent with the scaling relationship of Paper I. We therefore disagree with the statement in G96 that the flaring emission in dMe stars arises from compact loop structures.

The long flare loops result in mean coronal densities between  $10^9$  and  $10^{11}$  cm $^{-3}$ . The densities and loop lengths are similar to those we obtain from our loop models for the much larger flares on AU Microscopii (Cully et al. 1993) observed by *EUVE* during 1992 July ( $10^{10}$ – $10^{11}$  cm $^{-3}$ ; see Table 3 of Paper I). While it is possible that the flare mecha-

nism and coronal geometry of the AU Mic flares were entirely different from the flares on AD Leo, it is interesting that the densities and loop lengths derived from the models were similar (the difference in flare emission measure between the two stars is due primarily to a difference in flare area coverage according to the loop models). In principle, the densities we derive can be compared with those obtained from “density-sensitive” line ratios. The AD Leo spectra discussed in this paper are too noisy to yield meaningful results from such an analysis, but the AU Mic flares did have density-sensitive line pairs that were observed and analyzed. Monsignori Fossi et al. (1996) found that the flares on AU Mic could best be explained by small loops with densities of  $10^{12}$ – $10^{13}$   $\text{cm}^{-3}$  based on the density-sensitive Fe xxI 142 Å/128 Å line ratio. Schrijver et al. (1995) also found similarly high densities as a result of their analysis of the entire AU Mic spectra using the Fe xxI 142 Å/128 Å, Fe xxI 145 Å/128 Å, Fe xxI 103 Å/128 Å, and Fe xxII 114.4 Å/117.2 Å line ratios. In our view, such high densities would result in the flare plasma cooling during the decay phase far more rapidly than is observed from the EUVE DS light curves. It is not clear why the two density determinations disagree, but we believe a likely explanation for it lies in the work of Judge et al. (1997), who, based on estimates of the errors in the plasma model codes, the relatively weak dependence of the kernel functions on density, and the assumptions used in the method, have raised serious doubts about the validity of density-sensitive line ratios.

### 7.3. DEM Structure

The DEM structure shows clear differences in the quiescent, flare and decay phases. Figure 6 (*top panel; bottom panel* for the lower [Fe/H]) illustrates that the DEM is rather sharply peaked at a high temperature during F1 and at a cooler temperature during D while the Q DEM has a broad distribution encompassing a range of temperatures.

The loop models we developed in Fisher & Hawley (1990) provide insight into the origin of these DEM properties. We have computed the DEM for those loop models and find that it increases with temperature and is strongly peaked at the apex temperature of the loop. The DEM distribution with temperature can thus be approximated as a superposition of emission from loops with differing apex temperature. The results from the current paper can then be interpreted as follows. The Q DEM includes contributions from a broad temperature range at fairly low emission measure and suggests a broad distribution of loops with different apex temperatures. The F1 (and F2, but the data are significantly noisier during F2) DEM is more narrowly peaked at high temperature and large emission measure, indicating that the emission is dominated by one or a few hot loops with increased density due to chromospheric evaporation. The D DEM is also narrowly peaked but at lower temperature and emission measure; the emission may be coming from the same loops as during F1, but the loops have now cooled and much of the material has condensed back into the chromosphere.

Our data are not sufficient to distinguish between the G96 model, which includes two distinct (in temperature) populations of loops, and a model that includes a broad distribution of loops with apex temperatures covering a wide temperature range. In particular, the lack of strong lines that are formed at temperatures between  $\sim 10^{6.4}$  and

$10^{6.8}$  K in our spectra means that we have limited information about the extent of plasma at those temperatures. We note that recent work by Ciaravella, Maggio, & Peres (1996) and Griffiths (1996) shows that the identification of two populations of loops from two-temperature fits of ROSAT PSPC observations can be misleading; clearly better data will be required to address the loop apex temperature distribution during stellar flares.

## 8. CONCLUSIONS

We extracted EUV spectra from the star AD Leo during periods of quiescence, flaring, and during a period of flare decay. During all periods, the EUV spectra are dominated by Fe line emission (see Table 1) from temperatures ranging from  $\sim 10^6$  to  $10^7$  K, indicating that EUV emission from AD Leo is predominantly from a hot coronal plasma.

We modified the regularized inversion technique (Craig & Brown 1986; Mewe et al. 1995) to derive the differential emission measure (DEM) distribution of the corona. We introduce a weighting function for the data that depends not only on data quality (i.e., estimated errors in the spectrum) but also on the plasma emissivity function itself so that data at wavelengths coinciding with strong emission lines can be emphasized in the inversion procedure. This weighting is necessary to accommodate the low S/N of most spectral pixels in the AD Leo data. The inversion procedure can also be used (in principle) to determine coronal abundances and the interstellar hydrogen column density  $N_{\text{H}}$ . We have successfully tested the procedure with spectra generated from known test DEM distributions and can recover the DEM from the spectra (although the faithfulness of the inversion declines as the S/N decreases).

We applied this inversion technique to the AD Leo data and found DEM distributions generally consistent with those determined using the Pottasch method. We were unable to determine [Fe/H] for AD Leo because we have no positive detection of continuum emission, but we did find a value for  $N_{\text{H}}$  of  $(3 \pm 1) \times 10^{18} \text{cm}^{-2}$ .

During quiescence, we found a broad distribution of the DEM at temperatures from  $10^{6.8}$  to  $10^{7.2}$  K and also detected emission from temperatures near  $10^{6.2}$  K but with much lower DEM. We interpret the quiescent emission as being from a distribution of coronal loops with peak temperatures  $\sim 10^{6.8}$  to  $10^{7.2}$  K. Our conclusions differ from those of G96, who found an emission measure near  $10^{6.5}$  K within a factor of two of that at  $10^7$  K; we believe the difference is caused by the high value of  $N_{\text{H}}$  and low value of [Fe/H] that G96 used in their analysis.

During periods of flaring, we found that the variability was concentrated in the emission from temperatures near  $10^7$  K and that emission from lower temperatures remained nearly constant, in agreement with the results of G96.

The peak coronal temperature from the DEM analysis is significantly less for the large flare (F1;  $T_{\text{A}} \sim 1.3 \times 10^7$  K) than the value we used in Paper I ( $T_{\text{A}} \sim 2.5 \times 10^7$  K). This results in a lower coronal pressure and larger area coverage (Tables 4 and 5) for the coronal loops than the values quoted in Paper I (cf. Table 3 of Paper I). The value of [Fe/H] can also affect the derived loop parameters as discussed in § 7.2. Nevertheless, the basic conclusions of Paper I remain unchanged: the characteristic flare loop length on the star is long ( $L \sim R_{*}$ ), as determined by the flare rise and decay timescales ( $L \sim \tau_r^{3/7} \tau_d^{4/7} T_{\text{A}}^{1/2}$ ), with coronal densities between  $10^9$  and  $10^{11}$   $\text{cm}^{-3}$  at flare peak. Since the predict-

ed relationship between loop length and flare timescales has been tested for solar flares and found to be consistent with this relationship (Metcalf & Fisher 1996), we conclude that long loops on flare stars are consistent with the dynamical behavior of solar flare loops. This contrasts with the G96 conclusion that consistency with the solar analogue argues for short flare loops on AD Leo.

After the large flare F1, we observed a decrease in both peak temperature and emission measure during an extended decay phase. We interpret this as the gradual cooling and condensing of the flare plasma back to chromospheric temperatures as discussed in Paper I. (Another possibility is that we are observing the expansion and cooling of a hot coronal mass ejection; Cully et al. 1994.) Near the end of the decay phase, a second flare was

observed (F2), but the duration of the flare was short, resulting in a very low S/N for the spectrum and, consequently, a very uncertain DEM distribution.

We thank M. Abbott, M. Giampapa, N. Griffiths, C. Schrijver, and O. H. W. Siegmund for useful discussions. We especially thank T. Ayres for supplying a copy of his optimal extraction and line analysis code. We wish to thank the referee, B. van den Oord, for many helpful suggestions that improved the paper. S. L. C. was supported by NASA GSRP grant NGT-51062. G. H. F. was supported by NASA grants NAGW-3429 and NAGW-5133 and NSF grant AST 95-28474. S. L. H. was partially supported by NSF Young Investigator award 94-57455. T. S. acknowledges support from NASA grant NAG 5-2275.

#### REFERENCES

- Arnaud, M., & Raymond, J. C. 1992, *ApJ*, 398, 394  
 Arnaud, M., & Rothenflug, R. 1985, *A&AS*, 60, 425  
 Ayres, T. R. 1993, *PASP*, 105, 538  
 Brickhouse, N. S., Raymond, J. C., & Smith, B. W. 1995, *ApJS*, 97, 551  
 Ciaravella, A., Maggio, A., & Peres, G. 1996, *A&A*, 306, 553  
 Craig, I. J. D., & Brown, J. C. 1986, *Inverse Problems in Astronomy: A Guide to Inversion Strategies for Remotely Sensed Data* (Bristol: Adam Hilger Ltd.)  
 Cully, S. L. 1997, Ph.D. thesis, Univ. California, Berkeley  
 Cully, S. L., Fisher, G. H., Abbott, M. J., & Siegmund, O. H. W. 1994, *ApJ*, 435, 449  
 Cully, S. L., Siegmund, O. H. W., Vedder, P. W., & Vallerger, J. V. V. 1993, *ApJ*, 414, L49  
 Dennis, B. R., & Zarro, D. M. 1993, *Sol. Phys.*, 146, 177  
 Drake, J. J., Laming, J. M., & Widing, K. G. 1996, in *Astrophysics in the Extreme Ultraviolet*, ed. S. Bowyer & R. Malina (Dordrecht: Kluwer), 97  
 Feldman, U. 1992, *Phys. Scr.*, 46, 202  
 Fisher, G. H., & Hawley, S. L. 1990, *ApJ*, 357, 243  
 Fruscione, A., Hawkins, I., Jelinsky, P., & Wiercigroch, A. 1994, *ApJS*, 94, 127  
 Giampapa, M. S., Rosner, R., Kashyap, V., Fleming, T. A., Schmitt, J. H. M. M., & Bookbinder, J. A. 1996, *ApJ*, 463, 707 (G96)  
 Griffiths, N. W., Ph.D. thesis, Oxford Univ.  
 Gronenschild, E. H. B. M., & Mewe, R. 1978, *A&AS*, 32, 283  
 Hawley, S. L., et al. 1995, *ApJ*, 453, 464 (Paper I)  
 Horne, K. 1986, *PASP*, 98, 609  
 Judge, P. G., Hubeny, V., & Brown, J. C. 1997, *ApJ*, 475, 275  
 Malina, R. F., & Bowyer, S. 1991, in *Extreme Ultraviolet Astronomy*, ed. R. F. Malina & S. Bowyer (New York: Pergamon Press), 397  
 Metcalf, T. R., & Fisher, G. H. 1996, *ApJ*, 462, 977  
 Mewe, R., Kaastra, J. S., Schrijver, C. J., van den Oord, G. H. J., & Alkemade, F. J. M. 1995, *A&A*, 284, 477  
 Meyer, J.-P. 1991, *Adv. Space Res.*, 11(1), 269  
 Monsignori Fossi, B. C., & Landini, M. 1994a, *A&A*, 284, 900  
 ———. 1994b, *Sol. Phys.*, 152, 81  
 Monsignori Fossi, B. C., Landini, M., Del Zanna, G., & Bowyer, S. 1996, *ApJ*, 466, 427  
 Neupert, W. M. 1968, *ApJ*, 153, L59  
 Pottasch, S. R. 1963, *ApJ*, 137, 945  
 Press, W. H., Flannery, B. P., Teukolsky, S. A., & Vetterling, W. T. 1992, *Numerical Recipes* (Cambridge: Cambridge Univ. Press)  
 Raymond, J. C. 1995, in *Laboratory, Solar, and Stellar Astrophysical Plasmas*, ed. T. W. Hartquist & A. J. Willis (Dordrecht: Kluwer), 261  
 Raymond, J. C., & Smith, B. W. 1977, *ApJS*, 35, 419  
 Reid, I. N., Hawley, S. L., & Gizis, J. E. 1995, *AJ*, 110, 1838  
 Rumph, T., Bowyer, S., & Vennes, S. 1994, *AJ*, 107, 2108  
 Schmitt, J. H. M. M., Stern, R. A., Drake, J. J., & Kürster, M. 1996, *ApJ*, 464, 898  
 Schrijver, C. J., Mewe, R., van den Oord, G. H. J., & Kaastra, J. S. 1995, *A&A*, 302, 438  
 Siegmund, O. H. W., Vallerger, J., & Wargelin, B. 1987, in *IEEE Trans. Nucl. Sci.*, 35, 524  
 Stern, R. A., Lemen, J. R., Schmitt, J. H. M. M., & Pye, J. M. 1995, *ApJ*, 444, L45